Article
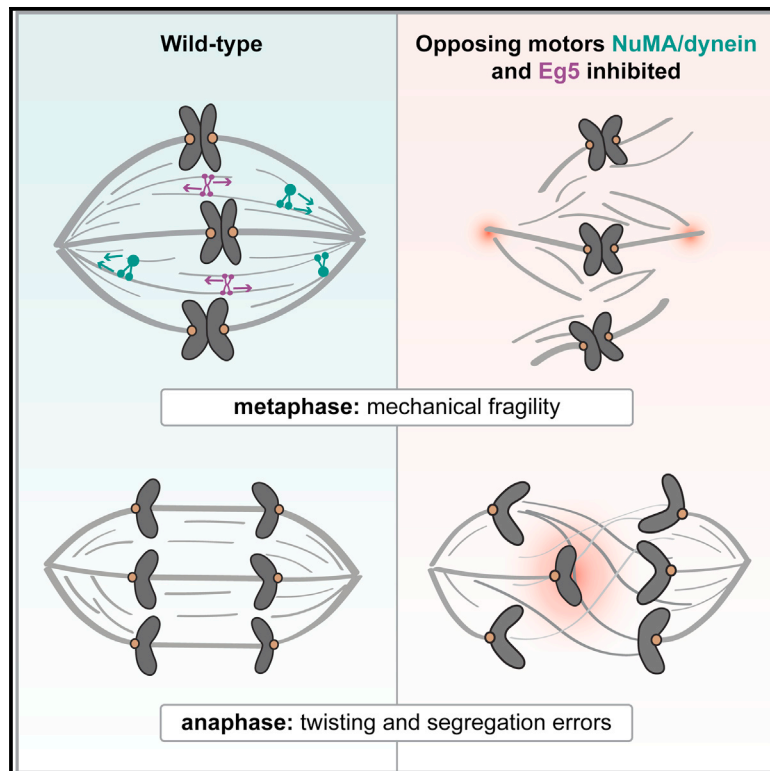
Opposing motors provide mechanical and functional robustness in the human spindle

Graphical abstract

Authors

Lila Neahring, Nathan H. Cho,
Sophie Dumont

Correspondence

sophie.dumont@ucsf.edu (S.D.),
lila.neahring@ucsf.edu (L.N.)

In brief

Successful cell division relies on the robust assembly of the microtubule-based spindle. Neahring et al. show that the opposing mitotic motors NuMA/dynein and Eg5 are not required for human spindle formation but are instead essential for its mechanical, structural, and functional robustness.

Highlights

- Spindles lacking NuMA/dynein and Eg5 motor activities attain normal shape and size

- Microtubule organization and flux are disrupted without these opposing motors

- Spindles lacking NuMA/dynein and Eg5 are mechanically fragile in metaphase

- Opposing forces are required to prevent twisting and segregation errors in anaphase

CellPress

Developmental Cell

CellPress

Article

Opposing motors provide mechanical and functional robustness in the human spindle

Lila Neahring,[1,2,*] Nathan H. Cho,[1,3] and Sophie Dumont[1,2,3,4,5,6,*]

[1]Department of Bioengineering & Therapeutic Sciences, UCSF, San Francisco, CA 94158, USA
[2]Developmental & Stem Cell Biology Graduate Program, UCSF, San Francisco, CA 94143, USA
[3]Tetrad Graduate Program, UCSF, San Francisco, CA 94158, USA
[4]Department of Biochemistry & Biophysics, UCSF, San Francisco, CA 94158, USA
[5]Chan Zuckerberg Biohub, San Francisco, CA 94158, USA
[6]Lead contact
*Correspondence: sophie.dumont@ucsf.edu (S.D.), lila.neahring@ucsf.edu (L.N.)
https://doi.org/10.1016/j.devcel.2021.09.011

SUMMARY

At each cell division, the spindle self-organizes from microtubules and motors. In human spindles, the motors dynein and Eg5 generate contractile and extensile stress, respectively. Inhibiting dynein or its targeting factor NuMA leads to unfocused, turbulent spindles, and inhibiting Eg5 leads to monopoles; yet, bipolar spindles form when both are inhibited together. What, then, are the roles of these opposing motors? Here, we generate NuMA/dynein- and Eg5-doubly inhibited spindles that not only attain a typical metaphase shape and size but also undergo anaphase. However, these spindles have reduced microtubule dynamics and are mechanically fragile, fracturing under force. Furthermore, they exhibit lagging chromosomes and a dramatic left-handed twist at anaphase. Thus, although these opposing motors are not required for spindle shape, they are essential to its mechanical and functional robustness. This work suggests a design principle whereby opposing active stresses provide robustness to force-generating cellular structures.

INTRODUCTION

At each cell division, the spindle self-organizes from dynamic microtubules, crosslinkers, and motors (Elting et al., 2018; McIntosh et al., 2012). Together, these molecular-scale force generators give rise to a cellular-scale structure with emergent properties, such as a steady-state shape in metaphase and the ability to accurately segregate chromosomes at anaphase. The mammalian spindle's molecular components have been extensively cataloged (Neumann et al., 2010), and the biophysical properties of many individual motors are now known. However, it remains poorly understood how combinations of motor activities—many of which act redundantly or in opposition to each other—give rise to the mammalian spindle's emergent architecture, mechanics, and function.

The motors Eg5 and dynein are key determinants of spindle architecture. Both generate directional forces between pairs of microtubules that they crosslink, building distinct cellular-scale motifs that coexist in the spindle's microtubule network. The kinesin-5 Eg5 (KIF11) is a bipolar homotetrameric motor that slides antiparallel microtubules apart, generating extensile stress in the spindle and maintaining pole separation (Blangy et al., 1995; Kapitein et al., 2005; Roostalu et al., 2018). Conversely, dynein is recruited to microtubule minus ends by its targeting factor NuMA, where it generates contractile stress by carrying minus end cargoes toward the minus ends of neighboring microtubules

(Figure 1A) (Foster et al., 2015; Gaglio et al., 1996; Hueschen et al., 2017). The activities of Eg5 and dynein are multifaceted and complex; for example, Eg5 also exerts braking forces in certain velocity regimes and between parallel microtubule pairs (Shimamoto et al., 2015), and dynein-mediated end clustering may require cooperative motor accumulation at microtubule minus ends (Tan et al., 2018). However, at the length scale of the spindle, these motors have opposing loss-of-function phenotypes that are deleterious for the dividing cell. When Eg5 is inhibited, spindles form as monopoles with minus ends clustered into a single aster (Mayer et al., 1999), whereas NuMA or dynein deletion leads to turbulent, disordered spindles with no steady-state shape and with microtubule bundles extending against the cell cortex (Hueschen et al., 2019).

Despite their importance to spindle architecture, when dynein and Eg5 are co-depleted, human spindles form as typical bipoles (Florian and Mayer, 2012; Hueschen et al., 2019; Tanenbaum et al., 2008; van Heesbeen et al., 2014). Similar phenomena have been reported in yeast, *Drosophila*, *Xenopus laevis* extract, and pig spindles when the homologous kinesin-5 and the dominant end-clustering motor (dynein or a kinesin-14) are inhibited (Ferenz et al., 2009; Mitchison et al., 2005; Rincon et al., 2017; Saunders and Hoyt, 1992; Sharp et al., 1999). These observations suggest that the balance of contractile and extensile stress in the spindle is more important than the specific magnitude of these stresses. This raises the
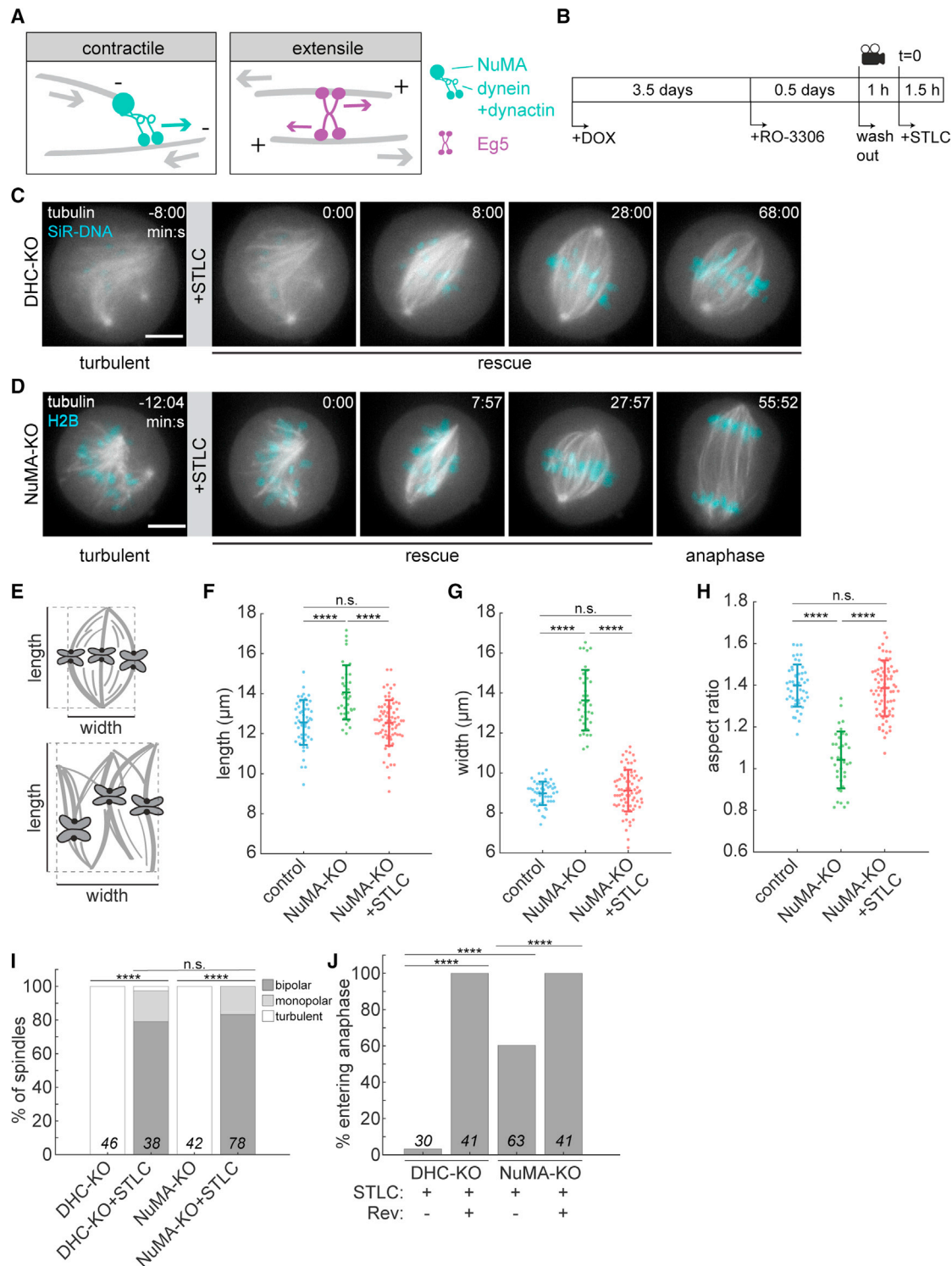
Figure 1. Eg5 inhibition allows turbulent spindles to recover bipolarity and progress to anaphase

(A) Schematic illustrations of contractile microtubule (gray filament) minus end clustering by dynein, dynactin, and NuMA (left, green), and extensile sliding of antiparallel microtubules by Eg5 (right, purple) in the human spindle. Dynein/dynactin, targeted to minus end cargoes by NuMA, walks toward microtubule minus ends (denoted by "−"). Eg5 walks toward microtubule plus ends (denoted by "+"). The direction of motor stepping is indicated by green and purple arrows, and contractile and extensile stresses are indicated by gray arrows.

(B) Schematic diagram of opposing motor (NuMA/dynein and Eg5) inhibition experiment in human spindles. Cas9 expression was induced by doxycycline addition (+DOX) for 4 days to knock out dynein heavy chain or NuMA. Cells were synchronized in G2 (with Cdk1 inhibitor RO-3306) for 0.5 days before imaging, released into mitosis, and Eg5 was acutely inhibited during imaging with 5 μM STLC. See also Figure S1.

(legend continued on next page)

Developmental Cell
Article

CellPress

question of what roles these opposing, energy-consuming motor activities play in the spindle if the same structure can be formed without them. Previous work in *Xenopus* extract spindles has suggested a role for opposing activities of dynein and Eg5 in establishing the spindle's microtubule organization, mechanical integrity, and heterogeneity (Brugués et al., 2012; Mitchison et al., 2005; Takagi et al., 2019), but it is unknown if this applies to other spindles, whose architectures differ and whose mechanics are challenging to probe. In human cells, the primary defect in dynein- and Eg5-doubly inhibited spindles is reported to be in kinetochore-microtubule attachments (van Heesbeen et al., 2014). However, dynein performs multiple functions at the kinetochore in addition to its role in minus end clustering (Howell et al., 2001; Raaijmakers and Medema, 2014), complicating the interpretation of dynein- and Eg5-doubly inhibited phenotypes in metaphase and limiting their study in anaphase. Thus, antagonistic contractile and extensile stress generation is a highly conserved feature of the spindle, but its mechanical and functional roles throughout the spindle's lifetime remain unclear.

Here, we show that although the opposing motor activities of NuMA/dynein and Eg5 are not required to build the human spindle, they are instead essential to its robustness—the spindle's ability to tolerate mechanical and biochemical fluctuations while maintaining its integrity and functional accuracy. Without these opposing motor activities, we find that spindles are more fragile when mechanically challenged in metaphase and highly twisted and error prone in anaphase. More broadly, these findings suggest a design principle by which opposing active force generators make self-organizing cellular structures robust.

RESULTS

Eg5 inhibition allows turbulent spindles to recover bipolarity and progress to anaphase

To generate human spindles lacking the opposing motor activities of NuMA/dynein and Eg5, we used an inducible CRISPR knockout (KO) approach (McKinley and Cheeseman, 2017) to delete either dynein heavy chain (DHC) or NuMA in RPE1 cells (Figures S1A–S1D). This results in chaotic, turbulent spindles that lose their long-range nematic order and constantly remodel, akin to active nematic materials *in vitro* (Hueschen et al., 2019;

Sanchez et al., 2012). This phenotype differs from the barrel-shaped spindles resulting from RNAi depletion of DHC (Tanenbaum et al., 2008) and from multipolar spindles, both of which reach a steady-state shape. We induced Cas9 expression for 4 days to knock out DHC or NuMA, synchronized cells with the Cdk1 inhibitor RO-3306, and released cells into mitosis before live imaging labeled microtubules and chromosomes to ensure that turbulent spindles did not accumulate defects during an extended mitotic arrest (Figure 1B). As previously reported, DHC-KO and NuMA-KO spindles exhibited a very similar turbulent phenotype, consistent with NuMA and dynein's acting as a complex to cluster microtubule minus ends (Hueschen et al., 2019, 2017). After confirming KO in each cell via spindle turbulence, we acutely inhibited Eg5 with S-trityl-L-cysteine (STLC), leading both DHC-KO and NuMA-KO spindles to recover into steady-state metaphase bipoles (Figures 1C, 1D, and S1E; Video S1). Many doubly inhibited spindles exhibited local defects that dynamically arose and repaired (Figure S1F), but in contrast to the expanded turbulent NuMA-KO spindles, global metaphase spindle shape and size was indistinguishable from that of the controls (Figures 1E–1H). The rescue and maintenance of bipolarity were highly reproducible and dependent on Eg5 inhibition (Figures 1I and S1G).

A key advantage of this experimental system was that many (60.3%) of the bipolar NuMA-KO+STLC spindles progressed to anaphase within 90 min of STLC addition. The rest remained in metaphase after 90 min, with no detectable sister chromatid separation or spindle elongation. In contrast, few (3.3%) of the DHC-KO+STLC spindles entered anaphase (Figure 1J). Consistent with dynein's NuMA-independent roles at the kinetochore in attachment formation and silencing the spindle assembly checkpoint (SAC) (Gassmann et al., 2010; Howell et al., 2001), bypassing the SAC using the MPS1 inhibitor reversine caused almost all NuMA- and DHC-KO+STLC cells to enter anaphase (Figure 1J). Due to these dynein-associated kinetochore defects and their confounding effects reported in previous studies of DHC- and Eg5-doubly inhibited spindles (van Heesbeen et al., 2014), we used NuMA-KO cells for the remainder of our experiments to isolate dynein's minus end clustering role. This approach provided us a system for probing the contributions of opposing motors to spindle mechanics and function in both metaphase and anaphase, independently of spindle architecture.

(C) Representative time-lapse confocal images of an RPE1 DHC-KO cell stably expressing GFP-tubulin (gray, maximum intensity projection of 5 planes) with SiR-DNA labeling chromosomes (cyan, single plane), starting as a turbulent spindle. After 5 μM STLC addition to inhibit Eg5 (time 0:00), the turbulent spindle recovers bipolarity but does not progress to anaphase. Scale bar, 5 μm.

(D) Representative time-lapse confocal images of an RPE1 NuMA-KO cell stably expressing GFP-tubulin (gray, maximum intensity projection of 5 planes) and mCherry-H2B (cyan, single plane), starting as a turbulent spindle. After 5 μM STLC addition to inhibit Eg5 (time 0:00), the turbulent spindle recovers bipolarity and progresses to anaphase. Scale bar, 5 μm.

(E) Schematic illustrations of spindle length and width measurements.

(F–H) Length (F), width (G), and aspect ratio (length/width; H) of the control (−DOX), turbulent NuMA-KO, and bipolar NuMA-KO+STLC spindles. Spindle dimensions were measured after the establishment of bipolarity (control, NuMA-KO+STLC) or 45 min after the start of imaging (NuMA-KO). Data in (F–H) include the same 49 (control), 36 (NuMA-KO), and 75 (NuMA-KO+STLC) spindles pooled from ≥3 independent experiments. ****p < 0.00005; n.s., not significant; two-sample t test. Error bars represent mean ± SD.

(I) Outcomes 90 min post-STLC addition to NuMA- and DHC-KO turbulent spindles. Without STLC addition, DHC-KO and NuMA-KO spindles remain turbulent. After STLC addition, most spindles establish bipolarity.

(J) Percentage of bipolar spindles entering anaphase within 90 min of STLC addition, with and without 500 nM of the MPS1 inhibitor reversine to bypass the SAC. DHC-KO+STLC cells enter anaphase after reversine addition, consistent with DHC-KO+STLC cells experiencing a SAC-dependent metaphase arrest. For (I and J), the number of spindles is indicated on each bar; cells pooled from ≥3 independent experiments. ****p < 0.00005, n.s., not significant; Fisher's exact test.
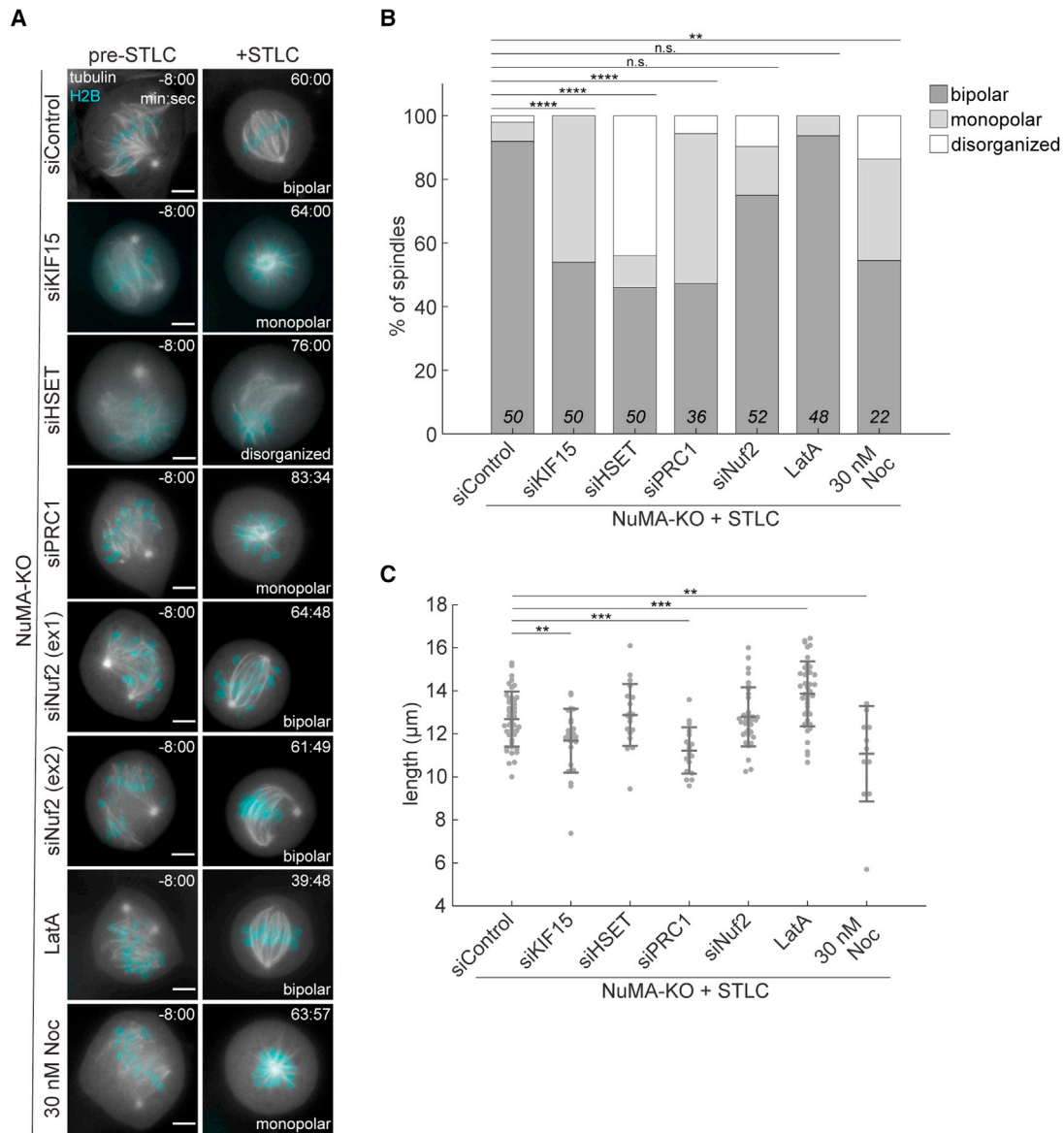
Figure 2. Doubly inhibited spindles are sensitized to changes in microtubule organization, dynamics, and motor-based forces

(A) Representative time-lapse confocal images of RPE1 NuMA-KO cells, stably expressing GFP-tubulin (gray, maximum intensity projection of 5 planes) and mCherry-H2B (cyan, single plane), and transfected with the indicated siRNA or treated with the indicated drug. 5 μM STLC was added at time 0:00 in each case, and 500 nM LatA and 30 nM nocodazole were added at time 0:00 where indicated. Scale bars, 5 μm. See also Figure S2.

(B) Spindle outcomes in NuMA-KO cells 90 min after STLC addition, with luciferase (control), KIF15, HSET, PRC1, or Nuf2 knockdown, 500 nM latrunculin A to disrupt actin, or 30 nM nocodazole to destabilize microtubules. The depletion of KIF15 or PRC1 and microtubule destabilization using low-dose nocodazole result in more monopolar spindles, whereas the depletion of HSET causes more spindles to remain disorganized. The number of spindles is indicated on each bar; cells pooled from ≥3 independent experiments. ****p < 0.00005; **p < 0.005; n.s., not significant; Fisher's exact test.

(C) Length of NuMA-KO+STLC spindles, transfected with the indicated siRNA or treated with the indicated drug, after the establishment of bipolarity. Data include the same spindles as (B), restricted to those scored as bipolar. Doubly inhibited bipoles are shorter on an average after KIF15 or PRC1 depletion or treatment with low-dose nocodazole and are longer on average after disruption of F-actin with latrunculin A. ***p < 0.0005; **p < 0.005, two-sample t test. Error bars represent mean ± SD.

Doubly inhibited spindles are sensitized to changes in microtubule organization, dynamics, and motor-based forces

Next, we asked what mechanisms allow turbulent spindles to establish bipolarity in the absence of NuMA/dynein and Eg5. We tested the contributions of additional candidate spindle fac-

tors representing several functional classes in the context of our live-imaged double-inhibition experiment. Partially depleting the kinesin-12 KIF15 in doubly inhibited spindles led to an increase in monopolar spindle formation (46%; Figures 2A, 2B, and S2A; Video S2), consistent with KIF15's known role in extensile stress generation (Sturgill and Ohi, 2013; van Heesbeen et al., 2014).

Developmental Cell
Article

CellPress

Similarly, depleting the microtubule crosslinker PRC1 or destabilizing microtubules with a low dose (30 nM) of nocodazole increased the frequency of monopolar spindles (Figures 2A, 2B, and S2B). In all three conditions, spindles that did achieve bipolarity were shorter on an average than doubly inhibited spindles transfected with non-targeting siRNA (Figure 2C). Abrogating kinetochore-fiber (k-fiber) formation via Nuf2 depletion did not significantly impact the frequency of bipolarization in doubly inhibited spindles, but we observed a variety of defects, including bent, over-bundled, and narrow spindles (Figures 2A, 2B, and S2C). None of these perturbations prevents bipolar spindle assembly in control cells (DeLuca et al., 2002; Polak et al., 2017; Tanenbaum et al., 2009; Vanneste et al., 2009), yet these data suggest that KIF15, PRC1, and dynamic microtubules all generate extensile stresses that are necessary for bipolarity in the absence of Eg5.

Conversely, depleting the kinesin-14 HSET caused more spindles to remain turbulent (44%; Figures 2A, 2B, and S2A; Video S2), indicating that it performs contractile minus end clustering redundantly with NuMA/dynein. F-actin was not required to focus minus ends during bipolarization, despite its importance in clustering supernumerary centrosomes (Kwon et al., 2008). Together, these triple inhibition experiments reveal that redundant motors and crosslinkers can generate bipolar spindles in the absence of NuMA and Eg5. However, these spindles are sensitized to changes in motor activity, microtubule organization, and dynamics—biochemical fluctuations to which the wild-type spindle is robust.

Microtubule organization and dynamics are disrupted in doubly inhibited spindles

Given that NuMA- and Eg5-doubly inhibited spindles are less robust to perturbations in microtubule organization and dynamics, we tested the hypothesis that internal architecture is disrupted in doubly inhibited spindles. We examined microtubule organization by quantifying the distribution of tubulin intensity along the spindle's pole-to-pole axis. As expected (Crowder et al., 2015), control cells had the strongest tubulin intensity near the two poles and lower intensity near the spindle equator. In contrast, tubulin intensity was more uniform in NuMA- and Eg5-doubly inhibited spindles (Figures 3A and 3B). This pattern was not due to a difference in chromosome alignment, as the intensity profile of the DNA stain Hoechst overlapped between the two conditions (Figure 3C). Thus, doubly inhibited spindles have altered microtubule organization, indicating that microtubule transport, nucleation, and/or length regulation in the spindle is disrupted without NuMA and Eg5.

Because both dynein and Eg5 are known to contribute to the continuous transport of non-kinetochore microtubules in the spindle (Lecland and Luders, 2014), we next asked whether the altered spatial distribution of microtubules in doubly inhibited spindles was associated with perturbed microtubule dynamics. We expressed photoactivatable-GFP-tubulin in NuMA-KO cells, co-labeled spindles with SiR-tubulin, and photoactivated stripes near the metaphase plate (Figure 3D; Video S3). Tracking photomark movements on individual k-fibers revealed that the poleward flux rate was halved in doubly inhibited spindles compared with that in controls (0.9 ± 0.5 μm/min compared with 1.8 ± 0.6 μm/min; Figure 3E). Although outward sliding by Eg5 drives

microtubule flux in *Xenopus laevis* extract spindles (Miyamoto et al., 2004), k-fiber flux in mammalian spindles is thought to be largely powered by mechanisms other than Eg5 (Cameron et al., 2006; Ganem et al., 2005; Steblyanko et al., 2020). However, our findings indicate that NuMA and Eg5 are together key to microtubule flux in the human spindle. We conclude that redundant motors and crosslinkers can establish the spindle's global shape and size without the opposing stresses generated by NuMA/dynein and Eg5 (Figure 2), but they cannot recapitulate its locally specialized microtubule organization and dynamics.

Doubly inhibited spindles are structurally unstable in response to mechanical force

Next, we tested the hypothesis that opposing motors contribute to the spindle's ability to maintain its structure under force. The loss of opposing NuMA/dynein and Eg5 activities could give rise to mechanical defects through reduced microtubule organization and dynamics (Figure 3) or through changes to the spindle's material properties as a result of altered local force generation. To probe the mechanics of NuMA- and Eg5-doubly inhibited spindles, we reproducibly confined metaphase cells in PDMS devices (Le Berre et al., 2012), forcing them into a flattened 5-μm-high geometry (Figure 4A). Doubly inhibited spindles exhibited a different characteristic response to confinement than controls, both in their deformation over time and in their loss of structural integrity (Figure 4B; Video S4). Although all spindles widened and lengthened during confinement, controls reached a new steady-state size after the first few minutes (Dumont and Mitchison, 2009), whereas doubly inhibited spindles continued to expand, failing to reach a new steady-state size in our observation period. During the initial expansion, spindles in both conditions widened similarly, but doubly inhibited spindles lengthened more slowly, consistent with a role of NuMA/dynein in spindle elongation (Guild et al., 2017). However, doubly inhibited spindles continued to grow in both dimensions throughout the perturbation, ultimately surpassing the new steady-state mean length and width of controls (Figures 4C and 4D). As another metric of spindle shape evolution, we calculated the 2D correlation coefficient between binarized masks of the same spindle at multiple timepoint pairs. The shape correlation of doubly inhibited spindles was lower than that of controls at increasing lag times, and exponential fits revealed that shape correlation decayed to a lower minimum value for doubly inhibited spindles (Figure 4E). Thus, under force, doubly inhibited spindles not only deform more but also have a weaker "shape memory" than controls.

Strikingly, the impaired ability of doubly inhibited spindles to stabilize their shapes was associated with increased structural failure. By 20 min after confinement onset, k-fibers had detached from poles in 91% of doubly inhibited spindles, compared with 25% of controls (Figures 4B and 4F). Although control spindle poles can split during sustained confinement (Lancaster et al., 2013), failure in doubly inhibited spindles began sooner and occurred more frequently (Figure 4F). Dynein- and Eg5-doubly inhibited spindles, but not Eg5-inhibited spindles, also failed during confinement more often than controls (Figure S3), indicating that the observed loss of mechanical integrity is due to a loss of opposing motor activity rather than due to Eg5 inhibition alone or
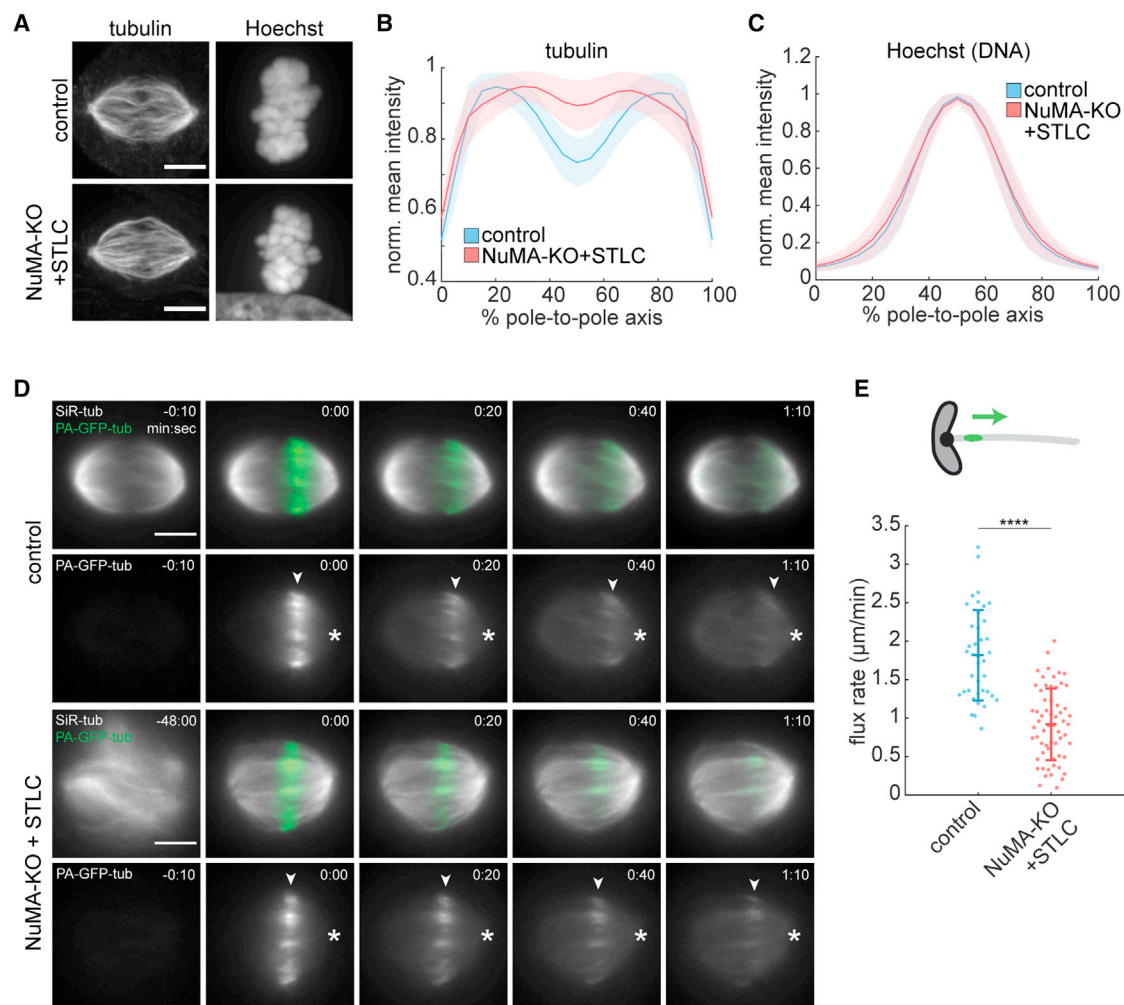
Figure 3. Microtubule organization and dynamics are disrupted in doubly inhibited spindles

(A) Representative immunofluorescence images (maximum intensity projections) of control and NuMA-KO+STLC RPE1 cells, stained for tubulin (left) and with Hoechst (right). Scale bars, 5 μm.

(B and C) Distributions of mean tubulin (B) and Hoechst (C) intensity at each point along the spindle's pole-to-pole axis, quantified from sum intensity projections of immunofluorescence images and normalized to the maximum value in each spindle (see STAR Methods). Doubly inhibited spindles have defects in microtubule organization. (B and C) include the same 335 control and 336 NuMA-KO+STLC cells pooled from 8 independent experiments. Plots represent mean ± SD.

(D) Representative time-lapse widefield images of RPE1 control and NuMA-KO+STLC cells stably expressing photoactivatable (PA)-GFP-tubulin (green), co-labeled with 100 nM SiR-tubulin (gray) and photomarked near the spindle equator (t = 0:00). The PA-GFP-tubulin channel alone is shown below the merged images. Arrowheads track the photomark position, and asterisks mark the spindle pole. Scale bars, 5 μm.

(E) Poleward flux rates in control and NuMA-KO+STLC cells, showing reduced microtubule transport in doubly inhibited spindles. Each dot represents an individual k-fiber. n = 39 k-fibers pooled from 14 cells in 1 experiment (control), n = 61 k-fibers pooled from 25 cells in 5 independent experiments (NuMA-KO+STLC). ****p < 0.00005, two-sample t test. Error bars represent mean ± SD.

any dynein-independent functions of NuMA. Moreover, the mode of failure qualitatively differed between doubly inhibited and control spindles: detached k-fibers in control spindles remained clustered into acentrosomal foci, but k-fibers in both NuMA- and DHC-KO doubly inhibited spindles splayed as individual bundles. Thus, although unperturbed doubly inhibited spindles maintain a similar geometry to controls (Figures 1F–1H), their reduced structural integrity becomes evident upon mechanical challenge. Together, the larger deformation, lack of new steady-state establishment, and structural fragility of doubly inhibited spindles under force indicate that the opposing motor ac-

tivities of NuMA/dynein and Eg5 are essential to the spindle's mechanical robustness.

Spindles with reduced opposing motor activity exhibit twist and functional defects in anaphase

Given that NuMA/dynein and Eg5 are together required for the metaphase spindle's internal organization, dynamics (Figure 3), and mechanical robustness (Figure 4), we next sought to determine whether they are important to anaphase spindle structure and function. Our finding that NuMA-KO+STLC spindles efficiently undergo anaphase (Figure 1), in contrast to DHC-KO+STLC
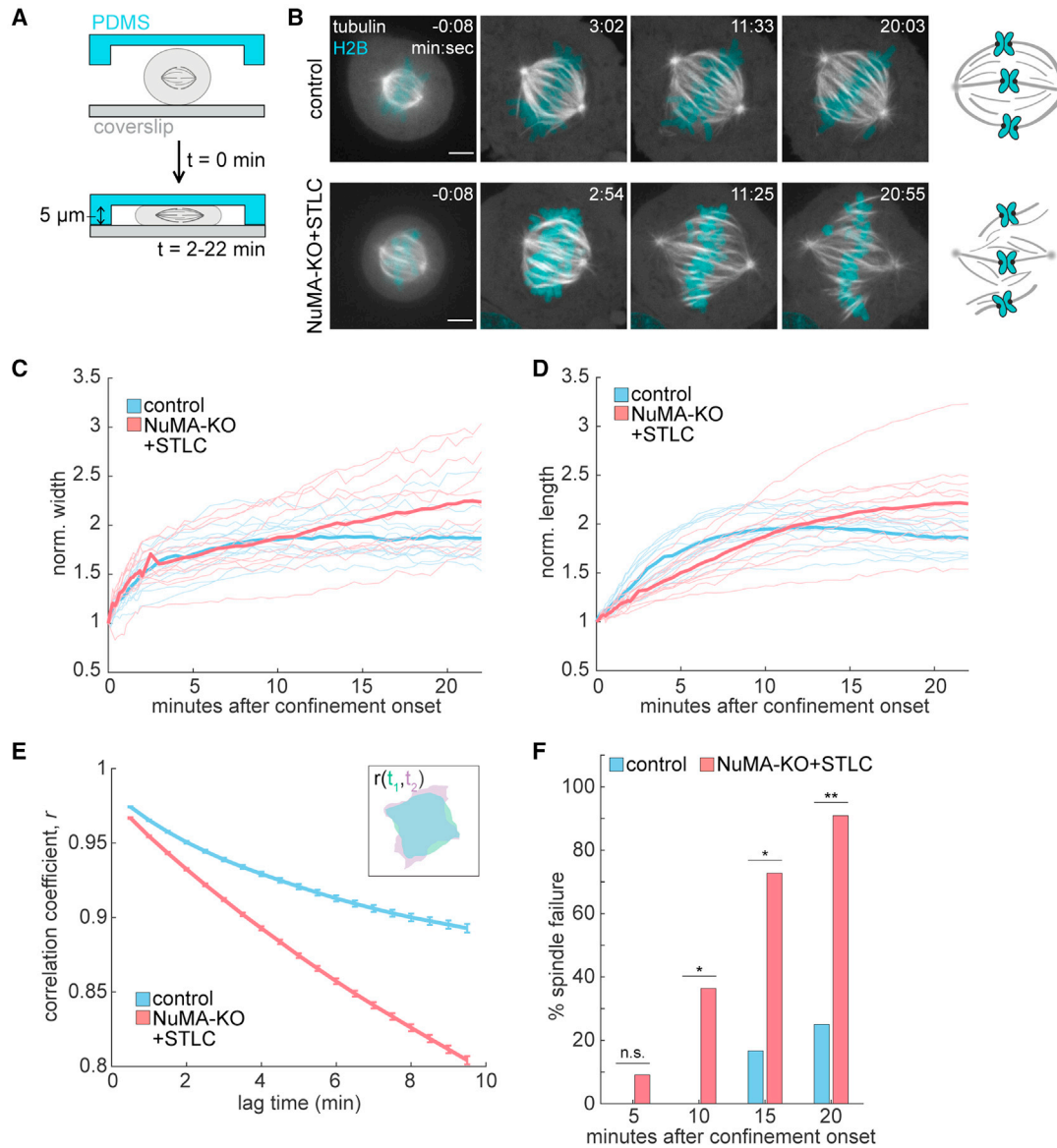
Figure 4. Doubly inhibited spindles are structurally unstable in response to mechanical force

(A) Schematic illustration of cell confinement experiment to probe spindle mechanical robustness. Confinement to 5 μm was applied over a period of 2 min, and the confined geometry was sustained for an additional 20 min.

(B) Time-lapse confocal images of control and NuMA-KO+STLC RPE1 cells stably expressing GFP-tubulin (gray) and H2B (cyan) during confinement (begins at t = 0:00). K-fibers detach from poles in the doubly inhibited spindle, whereas the control spindle remains intact, as cartooned (right). Scale bars, 5 μm.

(C and D) Spindle width (C) and length (D) during confinement of the control and NuMA-KO+STLC RPE1 cells, normalized to the initial length and width of each spindle. Mean values shown in bold lines. n = 12 control and 11 NuMA-KO+STLC cells, pooled from 5 and 4 independent experiments, respectively.

(E) Mean ± SEM of spindle shape correlation coefficient between all pairs of two binary, segmented frames (green t_1, purple t_2 in inset) as a function of the time elapsed between the two frames ($t_2 - t_1$). Shape correlation was fit to the exponential function $r = a * e^{\left(\frac{-1}{\tau}\right) * lag\ time} + b$, where $b = 0.87$ for controls and $b = 0.58$ for NuMA-KO+STLC. Analysis includes the same cells as (C and D).

(F) Percentage of spindles that structurally fail under confinement, defined qualitatively as a loss of continuity between k-fibers and poles. Doubly inhibited spindles begin to fail earlier, and fail more frequently, than controls. *p < 0.05; **p < 0.005; n.s., not significant; Fisher's exact test. Analysis includes the same cells as (C–E). See also Figure S3.

spindles, allowed us to address this question. In the first 3 min of anaphase doubly inhibited spindles elongated and chromosomes segregated at rates indistinguishable from controls (Figures 5A–5C, S4A, and S4B; Video S5). However, in doubly inhibited cells,

spindle elongation and chromosome segregation continued at these rates for extended durations, causing spindle poles to often hit the cortex and chromosomes to segregate to greater distances (Figures 5C, S4C, and S4D). Although cortical NuMA/dynein
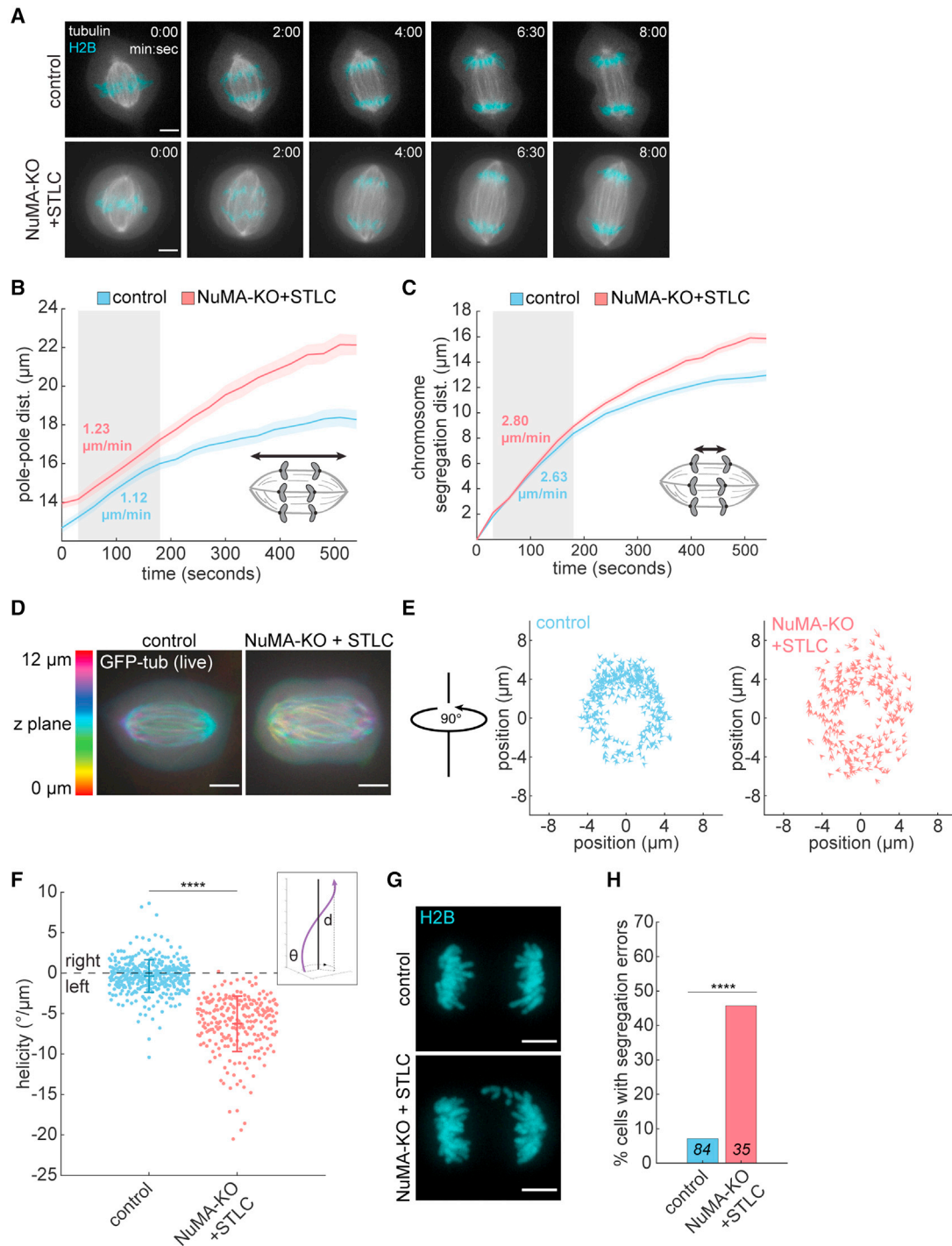
Figure 5. Spindles with reduced opposing motor activity exhibit twist and functional defects in anaphase

(A) Representative time-lapse confocal images of control and NuMA-KO+STLC RPE1 cells, stably expressing GFP-tubulin (gray) and H2B (cyan) during anaphase (begins at t = 0:00). Images represent a single z-plane. Scale bars, 5 μm.

(B) Spindle pole-to-pole distance during anaphase (aligned to anaphase onset at t = 0). Spindles initially elongate at indistinguishable rates (mean rates calculated over gray boxed area) but ultimately elongate more in doubly inhibited spindles. Lines and shaded regions indicate mean ± SEM of 20 cells (control) or 18 cells (NuMA-KO+STLC) pooled from 4 independent days. See also Figure S4.

(C) Distance between the two segregating chromosome masses in anaphase (anaphase onset at t = 0), same cells as (B). Chromosomes initially segregate at indistinguishable rates (mean rates calculated over gray boxed area) but segregate a greater total distance in doubly inhibited spindles. Lines and shaded regions indicate mean ± SEM. See also Figure S4.

complexes generate anaphase pulling forces in other systems (Aist et al., 1993; Grill et al., 2001), and although Eg5 has been reported to contribute to outward sliding during human spindle elongation (Vukušić et al., 2021), our results indicate that NuMA- and Eg5-doubly inhibited spindles are not deficient in elongation but instead over-elongate in anaphase. Thus, either doubly inhibited spindles are subject to increased outward forces in anaphase or they resist them less strongly.

Unexpectedly, we observed that, in contrast with control spindles and Eg5-inhibited spindles, doubly inhibited spindles were highly twisted in anaphase. Interpolar microtubule bundles followed a left-handed helical path around the spindle (Figure 5D). Although doubly inhibited spindles exhibited twist to a small degree at metaphase (Figures S5A and S5B), the phenotype was much more pronounced and consistently left handed after anaphase onset. To quantify this effect, we imaged z stacks of anaphase spindles and tracked interpolar microtubule bundles in three-dimensional space. Viewing these trajectories along the pole-to-pole axis, interpolar bundles in doubly inhibited spindles had a helicity of $-6.3° \pm 3.4°/\mu m$, a 17-fold increase over control bundles' helicity of $-0.4° \pm 2.0°/\mu m$ (mean ± SD; Figures 5E, 5F, and S5C; Video S6). Mean helicity was not correlated with anaphase spindle length (r = −0.04, Figure S5D), suggesting that spindle twist does not markedly increase or decrease as anaphase progresses. Together, these findings reveal an unexpected role for the opposing motor activities of NuMA/dynein and Eg5—although not required for linear force balance in the pole-to-pole axis (Figure 1F), they are required for rotational force balance in the anaphase spindle.

Finally, we asked whether chromosome segregation fidelity was preserved in doubly inhibited spindles. The incidence of chromosome segregation errors—defined here as lagging chromosomes or chromosome bridges—was significantly higher in NuMA-KO+STLC spindles than in controls (45.7% versus 7.1%; Figures 5G and 5H; Video S5). Thus, although NuMA and Eg5 are not required for efficient spindle elongation, they are instead required at anaphase for the spindle's straight long-range architecture and for accurate chromosome segregation.

DISCUSSION

The conserved presence of opposing extensile and contractile force generators, despite their expendability for bipolar spindle formation, presents a long-standing paradox in spindle assembly. Our use of direct mechanical perturbations, as well as our approach of deleting NuMA to preserve dynein's functions at the kinetochore, reveal key roles of this opposing motor activity. Although NuMA- and Eg5-doubly inhibited spindles appear strikingly similar to controls, they are mechanically fragile at metaphase as well as dramatically twisted and error prone at anaphase, defects that we propose stem from their altered dynamics, organization, and material properties (Figure 6). Although partially redundant motors can establish spindle shape and support anaphase progression, the opposing activities of NuMA/dynein and Eg5 are required to build a spindle that can maintain its structure and accurate function, despite internal and external pushes, pulls, and torques.

We show that mechanistically, the bipolarization of turbulent spindles after Eg5 inhibition requires the motors KIF15 and HSET, crosslinking by PRC1, and dynamic microtubules (Figure 2). KIF15 is known to compensate for the loss of Eg5 in forming and maintaining bipolar spindles, generating extensile stress through a mechanism distinct from that of Eg5 (Sturgill and Ohi, 2013; Tanenbaum et al., 2009; van Heesbeen et al., 2014; Vanneste et al., 2009). Although HSET has a mild loss-of-function phenotype in human cells (Cai et al., 2009), it forms microtubule asters in vitro (Mountain et al., 1999; Norris et al., 2018) and clusters centrosomes in cancer cells (Kwon et al., 2008), and our data suggest that it has a minus end clustering role that is unmasked in the absence of NuMA/dynein. Interestingly, fission yeast lacking all mitotic motors can form bipolar spindles that require the PRC1 homolog Ase1 and microtubule polymerization (Rincon et al., 2017). The similar requirements we observe in the absence of NuMA and Eg5 may reflect a conserved pathway for spindle assembly, based on microtubule bundling and polymerization, that complements the spindle's motor-driven microtubule sorting and becomes essential when motor activity is reduced.

NuMA and Eg5 are together essential to establishing the spindle's locally specialized microtubule organization and dynamics (Figure 3), roles that may explain the spindle's sensitivity to further molecular perturbations in their absence. The spindle's microtubule organization is established by spatially nonuniform distributions of microtubule nucleation and transport, and inhibition of Eg5 and NuMA/dynein could affect both activities. Eg5 and dynein are required to transport the nucleation factor TPX2 poleward in the mammalian spindle (Ma et al., 2010), and in their absence, microtubule nucleation may be shifted toward chromosomes. Eg5 and dynein both transport non-centrosomal microtubules toward poles (Brugués et al., 2012; Lecland and Luders, 2014), polarity sorting them and incorporating them into the spindle. Thus, in the absence of NuMA/dynein and Eg5, we propose that the spindle's tubulin intensity distribution is homogenized due to both deregulated microtubule nucleation and transport

(D) Representative confocal images of GFP-tubulin-labeled control (left) and NuMA-KO+STLC (right) RPE1 anaphase cells, showing a single time point from live imaging. Spindles are colored by z-plane. Scale bars, 5 μm.

(E) Spindle pole end-on views (90° rotation compared with view in D) of tracked interpolar microtubule bundles in control and NuMA-KO+STLC anaphase spindles. Arrow vectors represent the displacement of each bundle per μm traversed along the pole-to-pole axis, moving toward the viewer. n = 370 bundles, pooled from 40 cells in 5 independent experiments (control) and n = 238 bundles, pooled from 26 cells in 5 independent experiments (NuMA-KO+STLC).

(F) Helicity of individual interpolar microtubule bundles, measured in degrees rotated (Θ) around the pole-to-pole axis per μm traversed (d) along the pole-to-pole axis for each bundle. Schematic illustration of the helicity measurement shown in inset. Plot includes the same bundles tracked in (E). ****p < 0.00005, two-sample t test. Error bars represent mean ± SD. See also Figure S5.

(G) Representative confocal images of control and NuMA-KO+STLC RPE1 anaphase cells stably expressing GFP-tubulin (not shown) and mCherry-H2B (cyan, maximum intensity projections, single frame from live imaging), showing lagging chromosomes in the NuMA-KO+STLC cell. Scale bars, 5 μm.

(H) Percentage of anaphase cells with lagging chromosomes or chromosome bridges, showing increased segregation defects in NuMA-KO+STLC cells. n = 84 control cells pooled from 6 independent experiments; n = 35 NuMA-KO+STLC cells pooled from 5 independent experiments. ****p < 0.00005, Fisher's exact test.
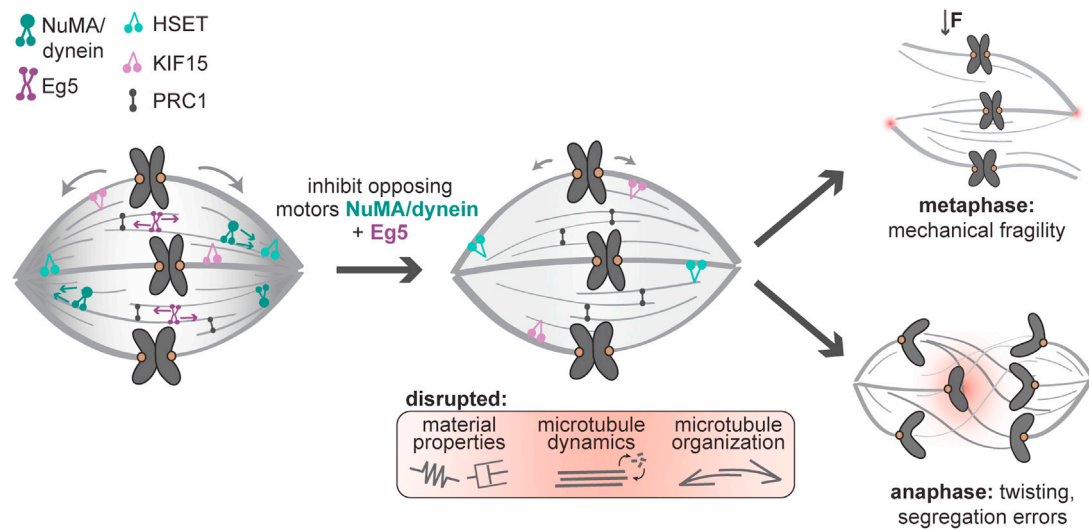
Figure 6. Model for opposing active stresses providing mechanical and functional robustness to the human spindle

The spindle has opposing contractile and extensile stresses generated by NuMA/dynein (dark green) and Eg5 (dark purple), respectively. Without these opposing active stresses (center), the human spindle retains its steady-state shape and size, due in part to the activities of the motors HSET (light green) and KIF15 (light purple) and the crosslinker PRC1 (black). However, these doubly inhibited spindles have reduced internal organization (gray gradient) and dynamics (gray arrows). These spindles are more structurally fragile when subjected to force at metaphase (top right), become highly twisted at anaphase, and exhibit chromosome segregation errors (lower right). We propose that opposing active stresses give rise to mechanical and functional robustness by increasing the spindle's microtubule organization and dynamics, and by tuning its material properties (springs, elasticity; dashpots, viscosity) to limit the magnitude and timescale of allowed deformations. Together, this work suggests a design principle whereby opposing active force generators promote mechanical and functional robustness of cellular machines.

toward poles. K-fiber flux in the human spindle is thought to arise from imperfect coupling of k-fibers to these non-kinetochore microtubules (Matos et al., 2009; Steblyanko et al., 2020), a model that would explain why we observe reduced k-fiber flux in doubly inhibited spindles.

We find that spindles are more mechanically fragile without opposing NuMA/dynein and Eg5 activity (Figure 4). This could stem from lower microtubule enrichment at poles (Figure 3B) (Takagi et al., 2019), a less dynamic spindle (Figure 3E), reduced passive crosslinking, or decreased active stresses throughout the spindle. All of these are ways in which reduced opposing motor activity could impair the spindle's ability to distribute and dissipate force, and thereby change the magnitude and timescale of the spindle's deformation under force. Motors broadly regulate the material properties of microtubule networks, such as their elasticity and viscosity (Brugués and Needleman, 2014; Shimamoto et al., 2011). In the future, combining the experimental system used here with approaches such as microneedle manipulation (Gatlin et al., 2010; Shimamoto et al., 2011; Suresh et al., 2020; Takagi et al., 2019) will enable us to understand how opposing motors quantitatively tune the spindle's emergent mechanical properties.

Our anaphase observations indicate that spindles have structural as well as functional defects without NuMA and Eg5. The efficient elongation of doubly inhibited spindles supports a model where Eg5-independent sliding within the spindle can generate the bulk of the force required for chromosome segregation (Vukušić et al., 2017, 2021; Yu et al., 2019). However, in contrast to controls, doubly inhibited anaphase spindles exhibit a strong left-handed twist, suggesting that they have an imbalance in torques. Multiple mitotic motors have an intrinsic chirality

to their stepping motion *in vitro* (Can et al., 2014; Mitra et al., 2018; Nitzsche et al., 2016; Yajima et al., 2008), which can twist microtubules around each other (Mitra et al., 2020). At the cellular scale, left-handed helicity of a smaller magnitude (approximately $-2°/\mu m$) exists in metaphase and anaphase human spindles, but this twist is reduced by Eg5 inhibition (Novak et al., 2018; Trupinic et al., 2020). Thus, as Eg5 is inhibited in the anaphase spindles probed here, a different mechanism must produce the left-handed torque. One possibility is that spindles lacking NuMA/dynein and Eg5 activity are twisted due to abnormally high torques generated by the motors that compensate for their absence. However, because doubly inhibited spindles are more mechanically deformable (Figure 4) and because they over-elongate in anaphase (Figure 5B), we favor a model in which they are instead more torsionally compliant. Regardless of its molecular origin, the appearance of twist upon inhibition of NuMA and Eg5 raises the question of how the cell builds a micron-scale, near-achiral spindle from nanometer-scale chiral events. This requires a balancing of three-dimensional rotational forces over large length scales, through mechanisms that remain poorly understood. The doubly inhibited spindles we generate here may provide a system to uncover these mechanisms and address the functional impact of twist in the anaphase spindle.

Doubly inhibited spindles exhibit a 6-fold increase in chromosome segregation errors. Decreased flux has been linked to attachment errors and lagging chromosomes in anaphase, through a mechanism that remains incompletely understood (Ganem et al., 2005; Matos et al., 2009); this phenomenon could be at play in doubly inhibited spindles, given their drastically reduced flux. Alternatively, lagging chromosomes could arise due to the assembly pathway of doubly inhibited spindles in

Developmental Cell
Article

CellPress

our assay. Since the NuMA- or DHC-KO spindles begin as turbulent networks before Eg5 inhibition, the minus end clustering process could lead to an elevated rate of merotelic attachment formation, similar to the attachment errors that arise during the clustering of supernumerary centrosomes (Ganem et al., 2009). In addition to either or both of these mechanisms, anaphase twist in doubly inhibited spindles could contribute to segregation errors. For example, segregating chromosomes might follow more complex, entangled trajectories, or the elongating spindle could generate an increased nonproductive force component that diminishes the spindle's ability to resolve merotelic attachments.

Overall, our findings indicate that the opposing activities of NuMA/dynein and Eg5 are critical for the spindle's mechanical and functional robustness, allowing the spindle to withstand force and accurately segregate chromosomes despite its dynamic molecular parts. An energy-accuracy trade-off has been demonstrated experimentally and theoretically in biochemical networks—for instance, repeated energy-consuming cycles of kinase and phosphatase activity synchronize cell-cycle timing in zebrafish embryos (Rodenfels et al., 2019) and phase coherence scales with energy dissipation in a variety of biochemical oscillators (Cao et al., 2015). We propose that opposing spindle motors provide a mechanical analog, where the spindle's structural integrity and functional accuracy incur an energetic cost beyond that required to establish spindle structure. Opposing active force generators may constitute a physical design principle that underlies robustness in other dynamic, self-organizing cellular structures, such as cell-cell junctions.

Limitations of the study

NuMA/dynein and Eg5 actively transport microtubules as they generate contractile and extensile stresses in the spindle, but also contribute to passive crosslinking by virtue of interacting with microtubule pairs. Eliminating this motor-mediated crosslinking, in addition to reducing opposing active stresses, could play a role in the defects we observe in doubly inhibited spindles. However, we find that STLC treatment alone increases mechanical robustness (Figure S3) and does not change anaphase twist (Figure S5C) compared with control spindles, rather than producing phenotypes intermediate between controls and doubly inhibited spindles. NuMA has also been proposed to have a dynein-independent passive crosslinking role (Forth et al., 2014). Although further work is required to define NuMA's contributions to passive and dynein-dependent crosslinking, we observe similar responses to confinement in doubly inhibited spindles generated via KO of NuMA or DHC (Figures 4F, S3B, and S3C). Thus, reduced crosslinking mediated by Eg5 or NuMA alone does not appear to play a substantial role in the mechanical fragility or anaphase twist we report in doubly inhibited spindles.

STAR★METHODS

Detailed methods are provided in the online version of this paper and include the following:

- KEY RESOURCES TABLE

- RESOURCE AVAILABILITY
  - Lead contact
  - Materials availability
  - Data and code availability
- EXPERIMENTAL MODEL AND SUBJECT DETAILS
- METHOD DETAILS
  - Transfection and small molecule treatments
  - Microscopy
  - Immunofluorescence
  - Western blotting
  - Cell confinement
- QUANTIFICATION AND STATISTICAL ANALYSIS
  - Quantification of spindle shape and failure
  - Quantification of NuMA levels
  - Fluorescence intensity profiles
  - Flux rate
  - Time correlation function of spindle shape
  - Anaphase segregation rates
  - Microtubule bundle helicity
  - Quantification of chromosome segregation errors
  - Statistical analysis

REFERENCES

Aist, J.R., Liang, H., and Berns, M.W. (1993). Astral and spindle forces in PtK2 cells during anaphase B: a laser microbeam study. J. Cell Sci. *104*, 1207–1216.

Blangy, A., Lane, H.A., d'Hérin, P., Harper, M., Kress, M., and Nigg, E.A. (1995). Phosphorylation by p34cdc2 regulates spindle association of human Eg5, a kinesin-related motor essential for bipolar spindle formation in vivo. Cell *83*, 1159–1169.

Brugués, J., and Needleman, D. (2014). Physical basis of spindle self-organization. Proc. Natl. Acad. Sci. USA *111*, 18496–18500.

Brugués, J., Nuzzo, V., Mazur, E., and Needleman, D.J. (2012). Nucleation and transport organize microtubules in metaphase spindles. Cell *149*, 554–564.

Cai, S., Weaver, L.N., Ems-McClung, S.C., and Walczak, C.E. (2009). Kinesin-14 family proteins HSET/XCTK2 control spindle length by cross-linking and sliding microtubules. Mol. Biol. Cell *20*, 1348–1359.

Cameron, L.A., Yang, G., Cimini, D., Canman, J.C., Kisurina-Evgenieva, O., Khodjakov, A., Danuser, G., and Salmon, E.D. (2006). Kinesin 5-independent poleward flux of kinetochore microtubules in PtK1 cells. J. Cell Biol. *173*, 173–179.

Can, S., Dewitt, M.A., and Yildiz, A. (2014). Bidirectional helical motility of cytoplasmic dynein around microtubules. Elife *3*, e03205.

Cao, Y., Wang, H., Ouyang, Q., and Tu, Y. (2015). The free energy cost of accurate biochemical oscillations. Nat. Phys. *11*, 772–778.

Crowder, M.E., Strzelecka, M., Wilbur, J.D., Good, M.C., von Dassow, G., and Heald, R. (2015). A comparative analysis of spindle morphometrics across metazoans. Curr. Biol. *25*, 1542–1550.

DeLuca, J.G., Moree, B., Hickey, J.M., Kilmartin, J.V., and Salmon, E.D. (2002). hNuf2 inhibition blocks stable kinetochore-microtubule attachment and induces mitotic cell death in HeLa cells. J. Cell Biol. *159*, 549–555.

Dumont, S., and Mitchison, T.J. (2009). Compression regulates mitotic spindle length by a mechanochemical switch at the poles. Curr. Biol. *19*, 1086–1095.

Elting, M.W., Suresh, P., and Dumont, S. (2018). The spindle: integrating architecture and mechanics across scales. Trends Cell Biol *28*, 896–910.

Ferenz, N.P., Paul, R., Fagerstrom, C., Mogilner, A., and Wadsworth, P. (2009). Dynein antagonizes Eg5 by crosslinking and sliding antiparallel microtubules. Curr. Biol. *19*, 1833–1838.

Florian, S., and Mayer, T.U. (2012). The functional antagonism between Eg5 and dynein in spindle bipolarization is not compatible with a simple push-pull model. Cell Rep *1*, 408–416.

Forth, S., Hsia, K.-C., Shimamoto, Y., and Kapoor, T.M. (2014). Asymmetric friction of nonmotor MAPs can lead to their directional motion in active microtubule networks. Cell *157*, 420–432.

Foster, P.J., Fürthauer, S., Shelley, M.J., and Needleman, D.J. (2015). Active contraction of microtubule networks. Elife *4*, e10837.

Gaglio, T., Saredi, A., Bingham, J.B., Hasbani, M.J., Gill, S.R., Schroer, T.A., and Compton, D.A. (1996). Opposing motor activities are required for the organization of the mammalian mitotic spindle pole. J. Cell Biol. *135*, 399–414.

Ganem, N.J., Godinho, S.A., and Pellman, D. (2009). A mechanism linking extra centrosomes to chromosomal instability. Nature *460*, 278–282.

Ganem, N.J., Upton, K., and Compton, D.A. (2005). Efficient mitosis in human cells lacking poleward microtubule flux. Curr. Biol. *15*, 1827–1832.

Gassmann, R., Holland, A.J., Varma, D., Wan, X., Civril, F., Cleveland, D.W., Oegema, K., Salmon, E.D., and Desai, A. (2010). Removal of spindly from microtubule-attached kinetochores controls spindle checkpoint silencing in human cells. Genes Dev *24*, 957–971.

Gatlin, J.C., Matov, A., Danuser, G., Mitchison, T.J., and Salmon, E.D. (2010). Directly probing the mechanical properties of the spindle and its matrix. J. Cell Biol. *188*, 481–489.

Grill, S.W., Gönczy, P., Stelzer, E.H., and Hyman, A.A. (2001). Polarity controls forces governing asymmetric spindle positioning in the Caenorhabditis elegans embryo. Nature *409*, 630–633.

Guild, J., Ginzberg, M.B., Hueschen, C.L., Mitchison, T.J., and Dumont, S. (2017). Increased lateral microtubule contact at the cell cortex is sufficient to drive mammalian spindle elongation. Mol. Biol. Cell *28*, 1975–1983.

Howell, B.J., McEwen, B.F., Canman, J.C., Hoffman, D.B., Farrar, E.M., Rieder, C.L., and Salmon, E.D. (2001). Cytoplasmic dynein/dynactin drives kinetochore protein transport to the spindle poles and has a role in mitotic spindle checkpoint inactivation. J. Cell Biol. *155*, 1159–1172.

Hueschen, C.L., Galstyan, V., Amouzgar, M., Phillips, R., and Dumont, S. (2019). Microtubule end-clustering maintains a steady-state spindle shape. Curr. Biol. *29*, 700–708.e5.

Hueschen, C.L., Kenny, S.J., Xu, K., and Dumont, S. (2017). NuMA recruits dynein activity to microtubule minus-ends at mitosis. Elife *6*, e29328.

Kapitein, L.C., Peterman, E.J., Kwok, B.H., Kim, J.H., Kapoor, T.M., and Schmidt, C.F. (2005). The bipolar mitotic kinesin Eg5 moves on both microtubules that it crosslinks. Nature *435*, 114–118.

Kwon, M., Godinho, S.A., Chandhok, N.S., Ganem, N.J., Azioune, A., Thery, M., and Pellman, D. (2008). Mechanisms to suppress multipolar divisions in cancer cells with extra centrosomes. Genes Dev *22*, 2189–2203.

Lancaster, O.M., Le Berre, M., Dimitracopoulos, A., Bonazzi, D., Zlotek-Zlotkiewicz, E., Picone, R., Duke, T., Piel, M., and Baum, B. (2013). Mitotic rounding alters cell geometry to ensure efficient bipolar spindle formation. Dev. Cell *25*, 270–283.

Le Berre, M., Aubertin, J., and Piel, M. (2012). Fine control of nuclear confinement identifies a threshold deformation leading to lamina rupture and induction of specific genes. Integr. Biol. (Camb) *4*, 1406–1414.

Lecland, N., and Lüders, J. (2014). The dynamics of microtubule minus ends in the human mitotic spindle. Nat. Cell Biol. *16*, 770–778.

Liu, D., Ding, X., Du, J., Cai, X., Huang, Y., Ward, T., Shaw, A., Yang, Y., Hu, R., Jin, C., and Yao, X. (2007). Human NUF2 interacts with centromere-associated protein E and is essential for a stable spindle microtubule-kinetochore attachment. J. Biol. Chem. *282*, 21415–21424.

Ma, N., Tulu, U.S., Ferenz, N.P., Fagerstrom, C., Wilde, A., and Wadsworth, P. (2010). Poleward transport of TPX2 in the mammalian mitotic spindle requires dynein, Eg5, and microtubule flux. Mol. Biol. Cell *21*, 979–988.

Matos, I., Pereira, A.J., Lince-Faria, M., Cameron, L.A., Salmon, E.D., and Maiato, H. (2009). Synchronizing chromosome segregation by flux-dependent force equalization at kinetochores. J. Cell Biol. *186*, 11–26.

Mayer, T.U., Kapoor, T.M., Haggarty, S.J., King, R.W., Schreiber, S.L., and Mitchison, T.J. (1999). Small molecule inhibitor of mitotic spindle bipolarity identified in a phenotype-based screen. Science *286*, 971–974.

McIntosh, J.R., Molodtsov, M.I., and Ataullakhanov, F.I. (2012). Biophysics of mitosis. Q. Rev. Biophys. *45*, 147–207.

McKinley, K.L., and Cheeseman, I.M. (2017). Large-scale analysis of CRISPR/Cas9 cell-cycle knockouts reveals the diversity of p53-dependent responses to cell-cycle defects. Dev. Cell *40*, 405–420.e2.

Meijering, E., Dzyubachyk, O., and Smal, I. (2012). Methods for cell and particle tracking. Methods Enzymol *504*, 183–200.

Mitchison, T.J., Maddox, P., Gaetz, J., Groen, A., Shirasu, M., Desai, A., Salmon, E.D., and Kapoor, T.M. (2005). Roles of polymerization dynamics, opposed motors, and a tensile element in governing the length of Xenopus extract meiotic spindles. Mol. Biol. Cell *16*, 3064–3076.

Mitra, A., Meißner, L., Gandhimathi, R., Renger, R., Ruhnow, F., and Diez, S. (2020). Kinesin-14 motors drive a right-handed helical motion of antiparallel microtubules around each other. Nat. Commun. *11*, 2565.

Mitra, A., Ruhnow, F., Girardo, S., and Diez, S. (2018). Directionally biased sidestepping of Kip3/kinesin-8 is regulated by ATP waiting time and motor-microtubule interaction strength. Proc. Natl. Acad. Sci. USA *115*, E7950–E7959.

Miyamoto, D.T., Perlman, Z.E., Burbank, K.S., Groen, A.C., and Mitchison, T.J. (2004). The kinesin Eg5 drives poleward microtubule flux in Xenopus laevis egg extract spindles. J. Cell Biol. *167*, 813–818.

Mountain, V., Simerly, C., Howard, L., Ando, A., Schatten, G., and Compton, D.A. (1999). The kinesin-related protein, HSET, opposes the activity of Eg5

Developmental Cell
Article

CellPress

and cross-links microtubules in the mammalian mitotic spindle. J. Cell Biol. *147*, 351–366.

Neumann, B., Walter, T., Hériché, J.K., Bulkescher, J., Erfle, H., Conrad, C., Rogers, P., Poser, I., Held, M., Liebel, U., et al. (2010). Phenotypic profiling of the human genome by time-lapse microscopy reveals cell division genes. Nature *464*, 721–727.

Nitzsche, B., Dudek, E., Hajdo, L., Kasprzak, A.A., Vilfan, A., and Diez, S. (2016). Working stroke of the kinesin-14, ncd, comprises two substeps of different direction. Proc. Natl. Acad. Sci. USA *113*, E6582–E6589.

Norris, S.R., Jung, S., Singh, P., Strothman, C.E., Erwin, A.L., Ohi, M.D., Zanic, M., and Ohi, R. (2018). Microtubule minus-end aster organization is driven by processive HSET-tubulin clusters. Nat. Commun. *9*, 2659.

Novak, M., Polak, B., Simunić, J., Boban, Z., Kuzmić, B., Thomae, A.W., Tolić, I.M., and Pavin, N. (2018). The mitotic spindle is chiral due to torques within microtubule bundles. Nat. Commun. *9*, 3571.

Pamula, M.C., Carlini, L., Forth, S., Verma, P., Suresh, S., Legant, W.R., Khodjakov, A., Betzig, E., and Kapoor, T.M. (2019). High-resolution imaging reveals how the spindle midzone impacts chromosome movement. J. Cell Biol. *218*, 2529–2544.

Polak, B., Risteski, P., Lesjak, S., and Tolić, I.M. (2017). PRC1-labeled microtubule bundles and kinetochore pairs show one-to-one association in metaphase. EMBO Rep *18*, 217–230.

Raaijmakers, J.A., and Medema, R.H. (2014). Function and regulation of dynein in mitotic chromosome segregation. Chromosoma *123*, 407–422.

Rincon, S.A., Lamson, A., Blackwell, R., Syrovatkina, V., Fraisier, V., Paoletti, A., Betterton, M.D., and Tran, P.T. (2017). Kinesin-5-independent mitotic spindle assembly requires the antiparallel microtubule crosslinker Ase1 in fission yeast. Nat. Commun. *8*, 15286.

Rodenfels, J., Neugebauer, K.M., and Howard, J. (2019). Heat oscillations driven by the embryonic cell cycle reveal the energetic costs of signaling. Dev. Cell *48*, 646–658.e6.

Roostalu, J., Rickman, J., Thomas, C., Nédélec, F., and Surrey, T. (2018). Determinants of polar versus nematic organization in networks of dynamic microtubules and mitotic motors. Cell *175*, 796–808.e14.

Sanchez, T., Chen, D.T., DeCamp, S.J., Heymann, M., and Dogic, Z. (2012). Spontaneous motion in hierarchically assembled active matter. Nature *491*, 431–434.

Saunders, W.S., and Hoyt, M.A. (1992). Kinesin-related proteins required for structural integrity of the mitotic spindle. Cell *70*, 451–458.

Schindelin, J., Arganda-Carreras, I., Frise, E., Kaynig, V., Longair, M., Pietzsch, T., Preibisch, S., Rueden, C., Saalfeld, S., Schmid, B., et al. (2012). Fiji: an open-source platform for biological-image analysis. Nat. Methods *9*, 676–682.

Sharp, D.J., Yu, K.R., Sisson, J.C., Sullivan, W., and Scholey, J.M. (1999). Antagonistic microtubule-sliding motors position mitotic centrosomes in Drosophila early embryos. Nat. Cell Biol. *1*, 51–54.

Shimamoto, Y., Forth, S., and Kapoor, T.M. (2015). Measuring pushing and braking forces generated by ensembles of Kinesin-5 crosslinking two microtubules. Dev. Cell *34*, 669–681.

Shimamoto, Y., Maeda, Y.T., Ishiwata, S., Libchaber, A.J., and Kapoor, T.M. (2011). Insights into the micromechanical properties of the metaphase spindle. Cell *145*, 1062–1074.

Steblyanko, Y., Rajendraprasad, G., Osswald, M., Eibes, S., Jacome, A., Geley, S., Pereira, A.J., Maiato, H., and Barisic, M. (2020). Microtubule poleward flux in human cells is driven by the coordinated action of four kinesins. EMBO J *39*, e105432.

Sturgill, E.G., and Ohi, R. (2013). Kinesin-12 differentially affects spindle assembly depending on its microtubule substrate. Curr. Biol. *23*, 1280–1290.

Suresh, P., Long, A.F., and Dumont, S. (2020). Microneedle manipulation of the mammalian spindle reveals specialized, short-lived reinforcement near chromosomes. Elife *9*, e53807.

Takagi, J., Sakamoto, R., Shiratsuchi, G., Maeda, Y.T., and Shimamoto, Y. (2019). Mechanically distinct microtubule arrays determine the length and force response of the meiotic spindle. Dev. Cell *49*, 267–278.e5.

Tan, R., Foster, P.J., Needleman, D.J., and McKenney, R.J. (2018). Cooperative accumulation of dynein-dynactin at microtubule minus-ends drives microtubule network reorganization. Dev. Cell *44*, 233–247.e4.

Tanenbaum, M.E., Macùrek, L., Galjart, N., and Medema, R.H. (2008). Dynein, Lis1 and CLIP-170 counteract Eg5-dependent centrosome separation during bipolar spindle assembly. EMBO J *27*, 3235–3245.

Tanenbaum, M.E., Macùrek, L., Janssen, A., Geers, E.F., Alvarez-Fernández, M., and Medema, R.H. (2009). Kif15 cooperates with Eg5 to promote bipolar spindle assembly. Curr. Biol. *19*, 1703–1711.

Thévenaz, P., Ruttimann, U.E., and Unser, M. (1998). A pyramid approach to subpixel registration based on intensity. IEEE Trans. Image Process. *7*, 27–41.

Trupinic, M., Ponjavic, I., Kokanovic, B., Barisic, I., Segvic, S., Ivec, A., and Tolic, I.M. (2020). Twist of the mitotic spindle culminates at anaphase onset and depends on microtubule-associated proteins along with external forces. bioRxiv. https://doi.org/10.1101/2020.12.27.424486.

van Heesbeen, R.G., Tanenbaum, M.E., and Medema, R.H. (2014). Balanced activity of three mitotic motors is required for bipolar spindle assembly and chromosome segregation. Cell Rep *8*, 948–956.

Vanneste, D., Takagi, M., Imamoto, N., and Vernos, I. (2009). The role of Hklp2 in the stabilization and maintenance of spindle bipolarity. Curr. Biol. *19*, 1712–1717.

Vukušić, K., Buda, R., Bosilj, A., Milas, A., Pavin, N., and Tolić, I.M. (2017). Microtubule sliding within the bridging fiber pushes kinetochore fibers apart to segregate chromosomes. Dev. Cell *43*, 11–23.e6.

Vukušić, K., Ponjavić, I., Buda, R., Risteski, P., and Tolić, I.M. (2021). Microtubule-sliding modules based on kinesins EG5 and PRC1-dependent KIF4A drive human spindle elongation. Dev. Cell *56*, 1253–1267.e10.

Yajima, J., Mizutani, K., and Nishizaka, T. (2008). A torque component present in mitotic kinesin Eg5 revealed by three-dimensional tracking. Nat. Struct. Mol. Biol. *15*, 1119–1121.

Yu, C.H., Redemann, S., Wu, H.-Y., Kiewisz, R., Yoo, T.Y., Conway, W., Farhadifar, R., Müller-Reichert, T., and Needleman, D. (2019). Central-spindle microtubules are strongly coupled to chromosomes during both anaphase A and anaphase B. Mol. Biol. Cell *30*, 2503–2514.

STAR★METHODS

KEY RESOURCES TABLE

REAGENT or RESOURCE	SOURCE	IDENTIFIER
Antibodies		
Mouse anti-α-tubulin	Sigma-Aldrich	Cat# T6199; RRID: AB_477583
Rat anti-α-tubulin	Bio-Rad	Cat# MCA77G; RRID: AB_325003
Rabbit anti-NuMA	Novus	Cat# NB500-174; RRID: AB_10002562
Mouse anti-α-tubulin conjugated to AF488	Cell Signaling Technology	Cat# 8058; RRID: AB_10860077
Alexa Fluor 568 goat anti-rabbit IgG	Thermo Fisher Scientific	Cat# A-11011; RRID: AB_143157
Alexa Fluor 647 goat anti-rabbit IgG	Thermo Fisher Scientific	Cat# A-21244; RRID: AB_2535812
Alexa Fluor 488 goat anti-rat IgG	Thermo Fisher Scientific	Cat# A-11006; RRID: AB_2534074
Alexa Fluor 488 goat anti-mouse IgG	Thermo Fisher Scientific	Cat# A-11001; RRID: AB_2534069
Rabbit anti-KIF15	Bethyl	Cat# A302-706A; RRID: AB_10748366
Mouse anti-KIFC1, Clone M-63	Santa Cruz Biotechnology	Cat# sc-100947; RRID: AB_2132540
Mouse anti-NDC80, Clone 9G3.23	Novus	Cat# NB100-338; RRID: AB_10000917
Mouse anti-PRC1, Clone 6G2	Biolegend	Cat# 629002; RRID: AB_2169531
Goat anti-mouse IgG-HRP	Santa Cruz Biotechnology	Cat# sc-2005; RRID: AB_631736
Mouse anti-rabbit IgG-HRP	Santa Cruz Biotechnology	Cat# sc-2357; RRID: AB_628497
Chemicals, peptides, and recombinant proteins		
Lipofectamine RNAiMAX Transfection Reagent	Thermo Fisher Scientific	Cat# 13778075
SiR-DNA kit	Cytoskeleton, Inc.	Cat# CY-SC007
SiR-tubulin kit	Cytoskeleton, Inc.	Cat# CY-SC002
RO-3306	Sigma-Aldrich	Cat# SML0569
(+)-S-trityl-L-cysteine	Sigma-Aldrich	Cat# 164739
Reversine	Sigma-Aldrich	Cat# R3904
Latrunculin A	Invitrogen	Cat# L12370
Nocodazole	Sigma-Aldrich	Cat# M1404
Hoechst 33342	Invitrogen	Cat# H3570
Critical commercial assays		
CellTiter-Glo Luminescent Cell Viability Assay	Promega	Cat# G7570
Experimental models: Cell lines		
Human: RPE1 inducible NuMA knockout cells	Hueschen et al., 2017	N/A
Human: RPE1 inducible dynein heavy chain knockout cells expressing GFP-tubulin	Hueschen et al., 2019	N/A
Human: RPE1 inducible NuMA knockout cells expressing GFP-tubulin and mCherry-H2B	This paper	N/A
Human: RPE1 inducible NuMA knockout cells expressing PA-GFP-tubulin	This paper	N/A
Oligonucleotides		
siRNA targeting Luciferase (control): 5'-CGUACGCGGAAUACUUCGA-3'	N/A	N/A
siRNA targeting KIF15: 5'-GGACAUAAAUUGCAAAUAC-3'	Vanneste et al., 2009	N/A
siRNA targeting HSET: 5'-UCAGAAGCAGCCCUGUCAA-3'	Cai et al., 2009	N/A
siRNA targeting PRC1: 5'-GUGAUUGAGGCAAUUCGAG-3'	Pamula et al., 2019	N/A
siRNA targeting Nuf2: 5'-AAGCAUGCCGUGAAACGUAUA-3'	Liu et al., 2007	N/A

Developmental Cell
Article

🔗 **CellPress**

Continued

REAGENT or RESOURCE	SOURCE	IDENTIFIER
Recombinant DNA		
pLenti6-GFP-tubulin	Laboratory of Torsten Wittmann (UCSF)	N/A
pLenti6-H2B-mCherry	Laboratory of Torsten Wittmann (UCSF)	Addgene plasmid #89766
pLenti-PA-GFP-tubulin	This study	N/A
Software and algorithms		
MetaMorph	Molecular Devices	7.10.3.279
FIJI	Schindelin et al., 2012	ImageJ 2.0.0-rc-69/1.52p
MTrackJ	Meijering et al., 2012	1.5.1
StackReg	Thévenaz et al., 1998	Version: July 7, 2011
MultiStackReg	Brad Busse (NIH)	1.45
MATLAB	MathWorks	R2020a
Other		
35 mm Dish, No. 1.5 Coverslip, Poly-D-Lysine coated	MatTek Life Sciences	Cat# P35GC-1.5-20-C

RESOURCE AVAILABILITY

Lead contact
Further information and requests for resources and reagents should be directed to and will be fulfilled by the Lead Contact, Sophie Dumont (sophie.dumont@ucsf.edu).

Materials availability
All unique cell lines generated in this study are available from the Lead Contact without restriction.

Data and code availability
Datasets and code generated for this study are available from the Lead Contact without restriction.

EXPERIMENTAL MODEL AND SUBJECT DETAILS

All cell lines were generated from an hTERT-RPE1 cell line (female human retinal epithelial cells) stably expressing neomycin-resistant tet-on SpCas9, a gift from I. Cheeseman (McKinley and Cheeseman, 2017). Cell lines additionally expressed a puromycin-selectable sgRNA targeting NuMA or dynein heavy chain (Hueschen et al., 2019). All cell lines were cultured at 37° and 5% CO_2 in DMEM/F12 (11320, Thermo Fisher) supplemented with 10% tetracycline-screened FBS (PS-FB2, Peak Serum). Fluorescently tagged proteins were introduced by transduction with blasticidin-resistant GFP-tubulin, mCherry-H2B, or PA-GFP-tubulin lentivirus, produced in HEK293T cells, supplemented with 10 μg/ml polybrene. Cell lines were selected with 5 μg/ml puromycin and 5 μg/ml blasticidin. SpCas9 expression was induced by the addition of 1 μg/ml doxycycline hyclate 4 days before each experiment, refreshed after 24 and 48 h.

METHOD DETAILS

Transfection and small molecule treatments
For siRNA knockdowns, cells were transfected with 50 pmol siRNA targeting luciferase as a negative control (5'-CGUACGCGG AAUACUUCGA-3', 48 h), HSET (5'-UCAGAAGCAGCCCUGUCAA-3', 48 h) (Cai et al., 2009), KIF15 (5'-GGACAUAAAUUGC AAAUAC-3', 24 h) (Vanneste et al., 2009), PRC1 (5'- GUGAUUGAGGCAAUUCGAG-3', 24h) (Pamula et al., 2019), or Nuf2 (5'- AAGCA UGCCGUGAAACGUAUA-3', 48h) (Liu et al., 2007) using Lipofectamine RNAiMAX (13778075, Thermo Fisher) according to the manufacturer's recommendations. Chromosomes were labeled in the inducible DHC-KO cell line (Figures 1C, 1I, and 1J) by incubating cells in 1 μM SiR-DNA and 10 μM verapamil (CY-SC007, Cytoskeleton Inc.) for 60 min prior to imaging. For photomarking experiments (Figures 3D and 3E), microtubules were labeled by incubating cells with 100 nM SiR-tubulin and 10 μM verapamil (CY-SC002, Cytoskeleton Inc.) for 60 min prior to imaging. For all experiments, cells were synchronized at the G2/M checkpoint by overnight treatment with 9 μM of the Cdk1 inhibitor RO-3306. Cells were released into mitosis by 4 washes in warm media, after which cells were imaged from prometaphase (controls, approximately 30 min after washout) or from reaching the turbulent state (NuMA- or DHC-KO, approximately 60 min after washout). Eg5 motor activity was inhibited by addition of S-trityl-L-cysteine (final concentration 5 μM or 40 μM as indicated, 164739, Sigma). For experiments where Eg5 was inhibited in wild-type cells, 5 μM

STLC was added to metaphase bipoles (Figure S3) or added at anaphase onset (Figure S5C). To bypass the spindle assembly checkpoint (Figure 1J), the MPS1 inhibitor reversine (final concentration 500 nM, R3904, Sigma) was added 45 min after STLC. F-actin and microtubules were disrupted (Figure 2) using Latrunculin A (final concentration 500 nM, L12370, Invitrogen) or nocodazole (final concentration 30 nM, M1404, Sigma-Aldrich), added at the same time as STLC. To measure cell viability, cells were plated in black-walled 96-well plates at 700 cells/well on day 0, doxycycline hyclate (1 μg/ml) was added to the media on the indicated days, and viability was measured on day 5 using the CellTiter-Glo assay (Promega) according to the manufacturer's instructions. Luminescence was detected using a Veritas Microplate Luminometer (Turner BioSystems).

Microscopy

For live imaging, cells were plated onto #1.5 glass-bottom 35 mm dishes coated with poly-D-lysine (P35G-1.5-20-C, MatTek Life Sciences) and imaged in a humidified stage-top incubator maintained at 37° and 5% CO_2 (Tokai Hit). Fixed and live cells were imaged on a spinning disk (CSU-X1, Yokogawa) confocal inverted microscope (Eclipse Ti-E, Nikon Instruments) with the following components: Di01-T405/488/561/647 head dichroic (Semrock); 405 nm (100 mW), 488 nm (150 mW), 561 nm (100 mW) and 642 nm (100 mW) diode lasers; ET455/50M, ET525/50M, ET630/75M, and ET705/72M emission filters (Chroma Technology); and a Zyla 4.2 sCMOS camera (Andor Technology). Images were acquired with a 100× 1.45 Ph3 oil objective using MetaMorph 7.10.3.279 (Molecular Devices). Photomarking experiments (Figures 3D and 3E) were performed on an OMX-SR inverted microscope (GE Healthcare) with the following components: three PCO Edge 5.5 sCMOS cameras; an environmental chamber maintained at 37° and 5% CO_2 (GE Healthcare); and a Plan ApoN 60× 1.42 oil objective. Photoactivation was performed with a single 20 ms pulse of 405 nm light targeted to a rectangular region of interest.

Immunofluorescence

For immunofluorescence, cells were plated onto acid-cleaned #1.5 25mm coverslips coated with 0.1% gelatin solution. Cells were fixed in methanol at -20°C for 3 min, washed with TBST (0.05% Triton-X-100 in TBS), and blocked with 2% BSA in TBST. Antibodies were diluted in TBST + 2% BSA and incubated overnight at 4°C (primary antibodies) or 45 min at room temperature (secondary antibodies). DNA was labeled with 1 μg/ml Hoechst 33342 for 20 min, prior to mounting on slides with ProLong Gold Antifade Mountant (P36934, Thermo Fisher). The following primary antibodies were used: mouse anti-α-tubulin (1:1,000, T6199, Sigma; RRID: AB_477583), rat anti-α-tubulin (1:500, MCA77G, Bio-Rad; RRID: AB_325003), rabbit anti-NuMA (1:300, NB500-174, Novus Biologicals; RRID: AB_10002562), and mouse anti-α-tubulin AlexaFluor 488 conjugate (1:50, added with secondary antibodies, 8058S, Cell Signaling Technology; RRID: AB_10860077). The following secondary antibodies were used at a 1:400 dilution: goat anti-rabbit AlexaFluor 568 and AlexaFluor 647 (A-11011 and A-21244, Thermo Fisher; RRID: AB_143157 and RRID: AB_2535812), goat anti-rat AlexaFluor 488 (A-11006, Thermo Fisher; RRID: AB_2534074), and goat anti-mouse AlexaFluor 488 (A-11001, Thermo Fisher; RRID: AB_2534069). Brightness/contrast for each channel was scaled identically within each immunofluorescence experiment shown.

Western blotting

Cells in 6-well plates were lysed, and protein extracts were collected after centrifugation at 4°C for 30 min. Protein concentrations were measured using a Bradford assay kit (Bio-Rad), and equal concentrations of each sample were separated on a 3-8% Tris-Acetate or 4-12% Bis-Tris gel (Invitrogen) by SDS-PAGE and transferred to a nitrocellulose membrane. Membranes were blocked with 4% milk, incubated in primary antibodies overnight at 4°C, and incubated with HRP-conjugated secondary antibodies for 1 h. Proteins were detected using SuperSignal West Pico or Femto chemiluminescent substrates (Thermo Fisher). The following primary antibodies were used: mouse anti-α-tubulin (1:5,000, T6199, Sigma; RRID: AB_477583), rabbit anti-NuMA (1:1,000, NB500-174, Novus Biologicals; RRID: AB_10002562), rabbit anti-KIF15 (1:500, A302-706A, Bethyl Laboratories; RRID: AB_10748366), mouse anti-KifC1 (M-63; 1:500, sc-100947, Santa Cruz Biotechnology; RRID: AB_2132540), mouse anti-NDC80 (1:500, NB100-338, Novus Biologicals; RRID: AB_10000917), and mouse anti-PRC1 (1:300, 629002, Biolegend; RRID: AB_2169531). The following secondary antibodies were used at a 1:10,000 dilution: goat anti-mouse IgG-HRP (sc-2005, Santa Cruz Biotechnology; RRID: AB_631736) and mouse anti-rabbit IgG-HRP (sc-2357, Santa Cruz Biotechnology; RRID: AB_628497).

Cell confinement

Cells were confined as described previously (Guild et al., 2017), using a suction cup device adapted from Le Berre et al. (2012). Briefly, PDMS pillars 5 μm in height (200 μm diameter, 700 μm spacing) were attached to a 10 mm-diameter coverslip, and were lowered onto cells using negative pressure generated manually using a 1 ml syringe. Pillars were gradually lowered onto cells over ~2 min, and maximum confinement (at a cell height of 5 μm) was sustained for an additional 20 min. Cells were excluded from analysis if the final confined height was >5 μm, suggesting that the cell's surroundings on the coverslip prevented full confinement, or if the separation between sister chromosomes became indistinguishable, suggesting chromosome decondensation, e.g. resulting from cell rupture.

QUANTIFICATION AND STATISTICAL ANALYSIS

Quantification of spindle shape and failure

Spindle length and width were measured manually using the line selection tool in FIJI (ImageJ version 2.0.0-rc-69/1.52p). For control and NuMA-KO+STLC cells, length was measured as the distance between the two spindle poles, and width was measured at the

Developmental Cell
Article

🔗 **CellPress**

widest part of the spindle across the metaphase plate. Aspect ratio was determined by dividing length by width. For turbulent NuMA-KO spindles and compressed spindles after structural failure, spindle axis directions were approximated from chromosome positions, and length and width were measured as the longest extent of spindle microtubules in these directions (see Figure 1E). For Figures 1F–1H, spindle dimensions were measured after reaching a bipolar metaphase (control and NuMA-KO+STLC) or 45 min after the start of imaging (NuMA-KO). For Figures 1I, 1J, and 2B, spindle architecture and anaphase entry were scored at 90 min after STLC addition, and cells that were imaged for <90 min were excluded. Spindle failure (Figures 4F and S3C) was defined as a loss of visible connectivity between k-fibers and the pole.

Quantification of NuMA levels

To compare NuMA intensity in control cells versus cells in which NuMA knockout had been induced, we quantified sum intensity projections of 21 z-planes spaced 0.35 μm apart. Using a custom MATLAB program (version R2020a), cell areas were segmented using a low tubulin threshold, and mean NuMA and tubulin intensities were measured within this region. NuMA intensities were normalized for each cell by dividing by the corresponding tubulin intensity. For the +DOX condition, only spindles with a disorganized phenotype (a single snapshot of a turbulent spindle) were analyzed, consistent with the criterion of spindle turbulence used for all live imaging experiments.

Fluorescence intensity profiles

Fluorescence intensity profiles along the pole-to-pole axis (Figures 3B and 3C) were quantified from sum intensity projections of 21 z-planes spaced 0.35 μm apart. Using a custom MATLAB program, images of tubulin fluorescence were passed through a median filter (3x3 pixels) and spindle areas were segmented using a tubulin intensity threshold. Based on the major axis angle of the segmented spindle, images were rotated so that the pole-to-pole axis was horizontal. At each of 21 positions (0%, 5%, 10%...100%) along the pole-to-pole axis, the mean tubulin and Hoechst intensities were calculated from the 1-pixel-wide column of all pixels contained within the spindle boundaries. Finally, these 21-point profiles were normalized to the maximum value for each spindle.

Flux rate

SiR-tubulin image sequences were aligned using a Rigid Body transformation, and the corresponding PA-GFP-tubulin image sequence was registered using the MultiStackReg plugin (version 1.45) to remove overall spindle drift. FIJI's segmented line selection tool with spline fitting was used to trace 2-3 k-fibers per spindle, and kymographs were generated from the PA-GFP-tubulin channel for each k-fiber using the Multi Kymograph plugin with a linewidth of 3 pixels. In MATLAB, the intensity values in each kymograph were smoothed with a moving mean calculated over a sliding 5-pixel window, and the position of maximum intensity was determined for each timepoint. Linear regression was performed on the positions of these maxima to determine the rate that the photomark moved polewards, using the MATLAB fit function of type 'poly1'.

Time correlation function of spindle shape

Timelapse image sequences were registered in FIJI using the Rigid Body option of the StackReg plugin (Thévenaz et al., 1998). Spindles were segmented in FIJI by smoothing, despeckling, background subtraction, and thresholding with Otsu's method. In MATLAB, thresholded binary image sequences were cropped to a 33x33 μm box centered at the spindle's centroid, and spindle masks were further refined by filling holes and removing small objects. The correlation coefficient was calculated, using the MATLAB corr2 function, between all pairs of binarized frames separated by lag time Δt, where Δt = 0.5, 1, 1.5, … 9.5 min. To determine shape correlation as a function of lag time, correlation coefficients were averaged for each lag time and fit to the exponential function $r = a * e^{\left(-\frac{1}{\tau}\right) * lag\ time} + b$ using MATLAB's curve fitting tool (Hueschen et al., 2019).

Anaphase segregation rates

Cells analyzed in Figures 5B, 5C, and S4 were imaged every 30 s from late metaphase through telophase. Anaphase onset was defined as the first frame with detectable chromosome separation. In each frame, the distance between the two spindle poles and the distance between the centers of the two chromosome masses were measured manually with the line selection tool in FIJI. Elongation and segregation rates were determined by linear regression of data between t = 30 s and t = 180 s, using the MATLAB fit function of type 'poly1'.

Microtubule bundle helicity

Helicity was analyzed similarly to the method described in Novak et al. (2018). We acquired z-stacks of GFP-tubulin-labeled spindles from live metaphase and anaphase cells. Z-axis calibration was performed using a FocalCheck slide #1 (F36909, Thermo Fisher), and the preservation of handedness throughout the optical train was validated by imaging a 3mm-diameter spring of known handedness with a 10× objective. Z-stacks were manually rotated in FIJI such that the pole-to-pole axis was horizontal. Image coordinates (x, y, z) were permuted to (z, x, y) in MATLAB, creating a series of spindle cross-sections as if viewed end-on from the pole (Video S6). The rotated image stacks were background-subtracted and despeckled to facilitate bundle tracking. Spindle poles were marked

and individual bundles were traced in FIJI using the MTrackJ plugin (Meijering et al., 2012), with cursor snapping to the bright centroid of a 15x15 pixel box enabled. In MATLAB, tracked bundle and pole positions were transformed so that both poles lay on the x-axis, accounting for spindle tilt. Tracked points were excluded if they lay outside the central 30-70% of the pole-to-pole axis. Bundles were excluded from further analysis if their mean radial distance from the central pole-to-pole axis was <2 μm, or if they contained fewer than 20 points (corresponding to a minimum track length of 1.16 μm). The angle between the first and last point in each bundle track was calculated with respect to the central pole-to-pole axis, and this angle was divided by the distance traversed along the pole-to-pole axis to calculate helicity.

Quantification of chromosome segregation errors
Segregation errors (Figures 5G and 5H) were determined from z-stacks of mCherry-H2B fluorescence, acquired with 1 μm spacing and covering the entire spindle height at a single timepoint during live imaging. Segregation errors included lagging chromosomes, defined here as one or more chromosomes completely separated from the rest of the chromosome mass, and chromosome bridges, defined here as an extended chromosome pair connecting the two segregating masses.

Statistical analysis
Details of statistical tests and sample sizes (number of cells and number of independent experiments) are provided in figure legends. Fisher's exact tests were performed to compare categorical datasets, using the fishertest function in MATLAB for 2x2 comparisons and the fisher.test function in R (version 4.0.1) for 2x3 comparisons. Two-sided two-sample t-tests were performed to compare continuous datasets using the ttest2 function in MATLAB, based on the assumption that spindle length and width, flux rate, anaphase segregation rate, and helicity are approximately normally distributed. We used $p < 0.05$ as the threshold for statistical significance. Linear regressions (Figures 3E, 5B, 5C, S4A, and S4B) and exponential decay fits (Figure 4E) were performed in MATLAB.